21st Australasian Fluid Mechanics Conference
Adelaide, Australia
10-13 December 2018

# Turbulent flow above wind-generated waves: conditional statistics and POD structures

**Kevin, J. Philip, J. H. Lee, T. Bhirawa and J. P. Monty**

Department of Mechanical Engineering, University of Melbourne, Victoria 3010, Australia

## Abstract

Large field-of-view particle image velocimetry (PIV) measurement is performed to characterise the turbulent boundary layer above evolving wind waves, which are developed over 3.5 m fetch at $U_\infty = 8.2$ m/s. This multi-camera experiment captures a streamwise domain of 0.4 m, slightly longer than two dominant wavelength of these wind waves. Instantaneous velocity observations reveal strong flow separations on the leeward side of most dominant waves, and these events are also marked by strong vertical velocity fluctuations. The spatially-averaged velocity profile further indicates a large velocity gradient below the wave crest, which occupies a significant proportion of the boundary layer. The conditionally-averaged flow fields around larger dominant waves show that turbulence stresses are high downwind the wave crest, indicating the highly varying form of the separation events. These events are further elucidated using proper orthogonal decomposition (POD) analysis, where the first few stronger modes reveal several common attributes around the separation events.

## Introduction

The momentum exchange between the air and sea influences many important parameters, such as the turbulence and temperature above the ocean, and the amplitude and wavelength of the sea waves. Hence, understanding the physical mechanisms of this exchange, as well as the complex interactions between sea waves, the turbulence in the water, and the surrounding air, is an active area of scientific research. Studying the interaction between the wind and the waves at the earlier stage of the wave formation is of a great importance, since their coupling mechanisms (along the thin air-water interface) determine the initial wave development. The resulting topography of the wind-generated waves has been shown to influence the air/sea momentum exchanges (Donelan *et al.* [1]).

For the wind-driven waves, where the wind speed is much faster than the wave propagation itself, the waves induce a pressure difference along the surface, causing form drag due to the surface elevation. As the slope of the wave gets steeper, airflow separations occur at the leeward face of the waves, indicating the 'onset' of wave breaking (Banner & Melville [2]). For shorter gravity waves, such as in the present study, Kawai [3] showed that wave folding/air entrainment is not requisite for the airflow separation to occur. Reul *et. al.* [5] related the form of the separation events with the instantaneous crest geometry, and concluded that front crest steepness is an important parameter.

The present study aims to carry out large-scale particle image velocimetry (PIV) measurement of airflow over wind-driven waves, and understand the flow separation. We also intend to identify the variation of events that will result in the turbulence-stress distribution.

## Experimental setup

### Wind-wave facility

The laboratory study is performed in a wind-wave facility in Michell Hydrodynamics Laboratory at the University of Melbourne. A schematic drawing of this facility is shown in figure 1 (drawn not to scale). The wave flume is 14 m long, 0.75 m wide and 0.7 m high, and filled with fresh water up to a depth of 0.3 m to satisfy the deep-water condition. This leaves 0.4 m high wind-tunnel test section up to the roof. A permeable sloped beach is placed at the downstream end of the flume to dissipate incoming waves, and hence reduces reflections. The glass walls of this tank enable full optical access to the test section. A suction-type wind tunnel is constructed on the upper part of the wave flume, where the wind is driven by a fan that can deliver up to 4.5 $m^3$/s of airflow. The tunnel entrance is fitted with a bell-mouth, which results in smooth flow intake. The flow then passes through a honeycomb flow-straightener and two perforated screens to further remove incoming larger-scale turbulence. A contraction with 3:1 area ratio then leads to the test section. The free-stream turbulence intensity $u_{rms}/U_\infty$ at the measurement station is nominally 0.5%.

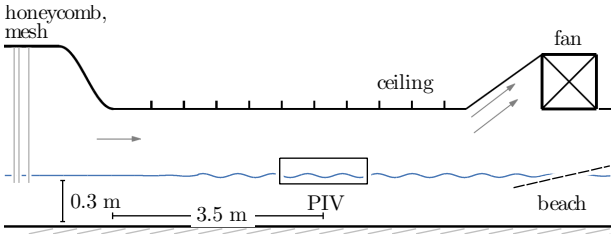


Figure 1: Schematic diagram of the wind-wave facility, highlighting its main features and the location of the PIV setup. The diagram is drawn not to scale.

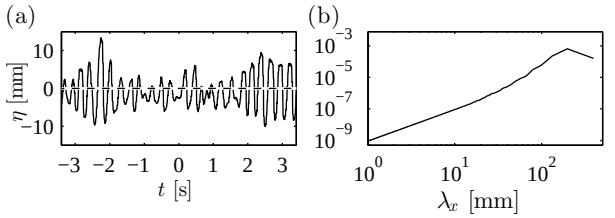


Figure 2: (a) Examples of wave-height temporal signals at 3.5 m fetch, for $U_\infty = 8.2$ m/s (or $U_{10} = 12.5$ m/s). Taken from single-point ultrasonic sensor. (b) The power spectral densities as function of wavelength $S_{\eta\eta}$ [mm], where the signals are taken from air-water interface captured in the PIV images.

### Surface roughness: wind-generated waves

The surface roughness considered here is the wind generated waves, developed over 3.5 m long fetch at a freestream velocity of $U_\infty$ = 8.2 m/s. Throughout this paper, $x$ and $z$ will denote the streamwise and vertical directions (referenced to the mean water depth), respectively. The wind-generated wave elevations are first characterised using General Acoustics USS02/HF ultrasonic sensors with a sampling rate of 100 Hz. Figure 2 shows examples of the water surface elevations $\eta$ and the corresponding surface elevation spectra.

The measured wind waves have a peak frequency $f_0 = 3.4$ Hz at this input wind speed. Here, the phase velocity of the dominant wave $C_0$ is measured directly by correlating simultaneous signals of two wave gauges which are separated by 72 mm. Divid-

| $U_\infty$ (m/s) | $f_0$ (Hz) | $C_0$ (m/s) | $\lambda_0$ (m) | $H_s$ (mm) |
|---|---|---|---|---|
| 8.2 | 3.4 | 0.67 | 0.18 | 19.6 |
| | $\delta$ (mm) | $U_*$ (m/s) | $z_0$ (mm) | $U_{10}$ (m/s) |
| | 113 | 0.48 | 0.14 | 12.6 |

Table 1: Top: wind-wave parameters, and bottom: boundary layer parameters. $f_0$: dominant phase frequency; $C_0$: celerity of the dominant phase; $\lambda_0$: dominant wavelength; $H_s$: significant wave height; $\delta$: boundary-layer thickness; $U_*$: friction velocity; $z_0$: roughness length; $U_{10}$: velocity extrapolated to 10 m height.

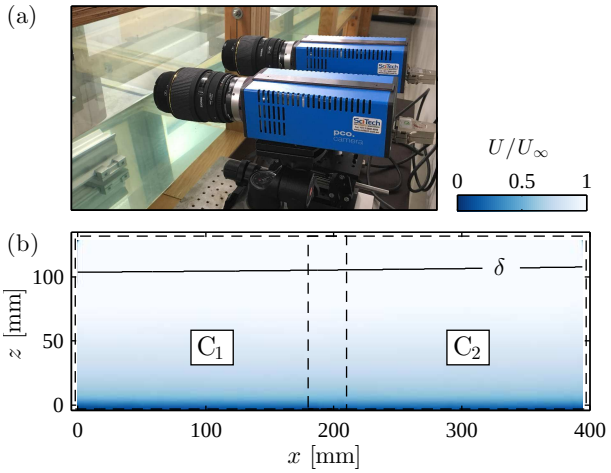


Figure 3: (a) Picture of the camera configuration used for the large-view PIV experiments. (b) The combined $x/z$ domain recorded by this setup. Dashed line: FOV of each camera. $\delta$ illustrates the mean boundary layer height.

ing this known distance by the cross correlation peak between the two wave height signals is used to directly measure the average convection speed of the most dominant wave phase. The experimental parameters for the surface waves are summarised in table 1. Since the wind-waves are developed over a relatively short fetch length (approximately 3.5 m), the wave age that indicates the wave development stages is $C_0/U_* \sim 1.5$ (or $U_{10}/C_0 \sim 18$). This implies that the wave fields are strongly forced by the local winds (Donelan *et. al.* [4])

## Large-view PIV experiments

In the present PIV experiment, the airflow is seeded with 1 µm-diameter polyamide particles, where they are illuminated by a 0.5 mm thick laser sheet generated by a Quantel EverGreen double-pulse Nd:YAG laser. The imaging system consists of two 14-bit PCO4000 (4008×2672 pixels) frame-straddled cameras. Pictures of the camera setups are displayed in figure 3(a) highlighting their 5° downward viewing angle. This arrangement is an attempt to reduce view obstruction due to the surface topography that may appear between the measurement plane and the camera sensors. This problem is known as the meniscus effect, and is inherent in all image-based wave measurements where the moving surface topography is three-dimensional. To compensate both lens and viewing-angle distortions, the PIV images are calibrated using a set of calibration dots, equispaced in the streamwise and vertical directions by 5 mm. Third-order polynomials are used to construct a mapping function between the image and real space. It is crucial to capture the calibration image when the water level is significantly lower than during the actual measurements, to ensure that the calibration grid covers the deepest trough of the waves, hence avoiding extrapolation in the reconstruction. The displacement evaluation and reconstruction is done using an in-house PIV package. The air-water interface is determined from the PIV images prior to computing the velocity vectors. The reconstructed field-of-view is illustrated in figure 3(b), highlighting the 0.4 m streamwise domain. Here both cameras $C_1$ and $C_2$ are equipped with Sigma 105 mm macro lenses, and yield a pixel resolution of 54 µm/px. Final interrogation window of $24 \times 24$ pixel is employed, and a total of 1200 reconstructed velocity realisations are acquired at a rate of 1 Hz.

### Instantaneous flow fields over wind-generated waves

Figure 4(a) displays an example of instantaneous streamwise velocity field over the wind waves, highlighting the strong turbulent behaviour within the present flow. The figure also demonstrates the large amplitude and wavelength of the wind waves ($\lambda_0 \approx 0.18$ m) as compared to the boundary layer thickness itself ($\delta = 0.11$ m). The extent of the roughness obstacles to the flow is further shown in the mean velocity profile (figure 4b), where the line of $3\sigma_\eta$ indicates the height of 'large wave crests'. The profile also shows the large velocity gradient within the wave crests. We plot the isocontour of $u = 0.95U_\infty$ over the instantaneous field, indicating the dip of the contour (i.e. instantaneous boundary layer is relatively thinner) above the wave crest, which is important to satisfy conservation of mass. Immediately above the surface, airflow separations occur downstream of most waves. Over the deformable water surface, separation events indicate the 'onset' of wave breaking (Banner & Melville [2]), although for shorter gravity waves, such as those we observe here, air entrainment/wave folding still can be prevented by the surface tension of the water (Banner & Peregrine [8]). The inset of figure 4(a) show the instantaneous vertical velocity around a wave crest. As shown by Buckley & Veron [10], in much slower wind speed, the airflow typically rides along the wave undulation creating an obvious uphill and downhill $w$ velocity on the windward and leeward side of the waves respectively. These 'wave coherent' motions describe a potential flow behaviour and not necessarily represents turbulent activity. For the higher wind speed such as shown in figure 4 however, the vertical velocity can appear to be less coherent with the wave phase, instantaneously at least, and the flow field is dominated by the increased smaller-scale $w$ events within the separation region. An intense vertical velocity fluctuation close to the air-water interface is known to be crucial for surface wave formation, momentum transfer, mixing and the exchange of energy and gases.

### Flow around average dominant waves

To statistically characterise the flow field around a wave crest (of the dominant wave), we reconstruct the average/representative wave with $\lambda_0 \sim 0.18$ m. As shown in figure 5(a), we only consider the instantaneous wave occurrences which have front steepness $a/\lambda_f$ of at least 0.17 as samples. The variation of all the instances considered is illustrated by the series of grey lines, where the surface which deviates too much from the mean shape has been discarded. A total of approximately 100 instances are used to construct the mean wave shape and to compute the velocity statistics. The resulting average dominant wave profile is shown by the thick line, where the wave crest is locked at $\Delta z = 0$. Figure 5(b, c) display the conditionally-averaged streamwise and vertical velocity fields (denoted by the angle brackets) respectively. It is evident that $\langle U \rangle$ velocity on the leeward side is lower than over the windward, as a result of the separation events due to strong adverse pressure gradient. Over the wave crest itself however, the airflow is relatively fast reaching $0.7U_\infty$. The general upward and downward trends are also apparent in $\langle W \rangle$, indicating the wave-coherent motions/fluctuations.

Figure 6(a, b) show the corresponding turbulence intensities relative to the mean field discussed above, where here $u' = u - \langle U \rangle$.

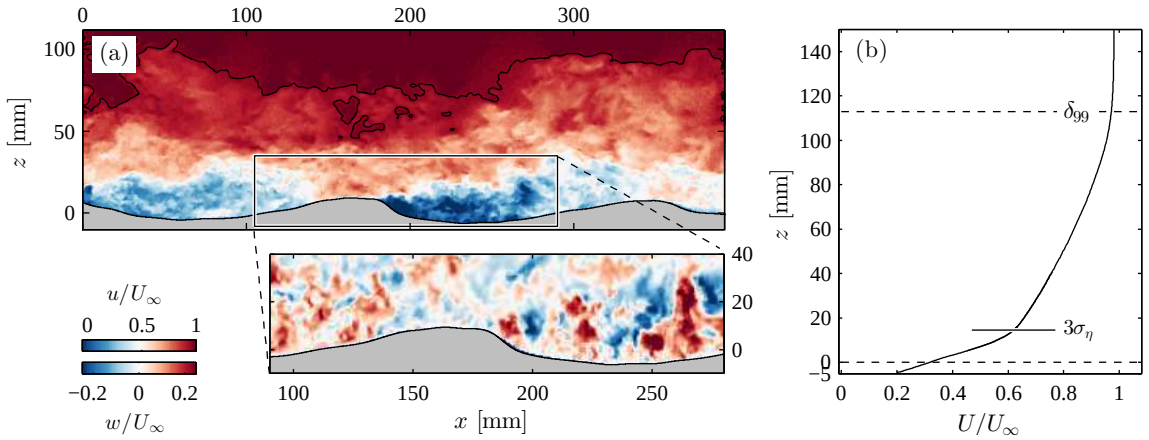


Figure 4: (a) Instantaneous streamwise velocity example from the present large-view PIV. Black contour line: $u = 0.95U_\infty$. Inset: vertical velocity within the highlighted section. (b) The corresponding mean velocity profile, obtained from separate PIV experiment.

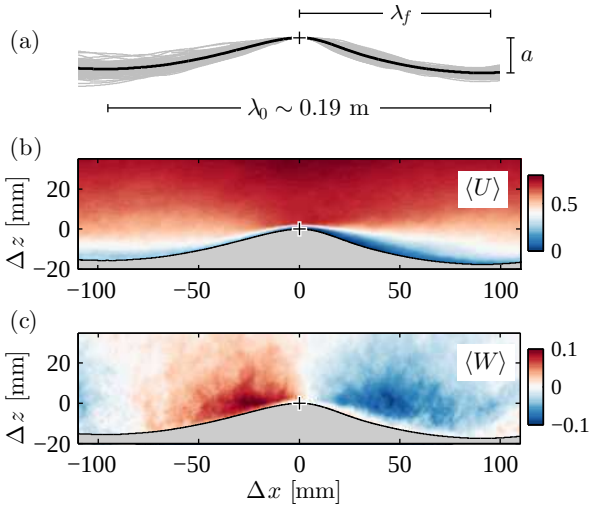


Figure 5: (a) Average dominant wave shape (thick line) for $a/\lambda_f > 0.17$. Grey lines: all the surface profiles included in the averaging. + symbol: averaging process is locked on the wave crest. (b, c) Conditionally-averaged streamwise $\langle U \rangle / U_\infty$ and wall-normal $\langle W \rangle / U_\infty$ velocity.

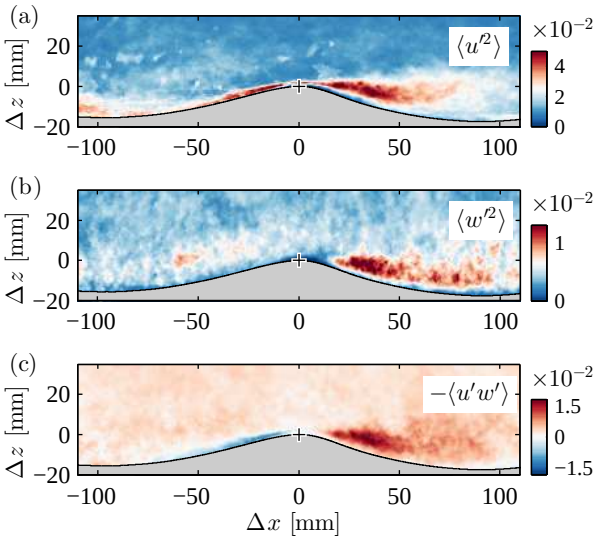


Figure 6: The corresponding turbulence stresses about the mean velocity represented in figure 5. (a) Streamwise $\overline{u'^2}/U_\infty^2$, (b) vertical $\overline{w'^2}/U_\infty^2$, (c) shear stress $-\overline{u'w'}/U_\infty^2$.

The intense quantity on the leeward gradient indicates the highly varying flow structure during separation event, including the loci of both separation and reattachment points. Similar to the observation made by Chan *et. al.* [9] over large (three-dimensional) sinusoidal roughness, the most intense streamwise turbulence intensity occur at the elevation of the wave crest. Figure 6(c) displays the shear stress quantity $-\langle u'w' \rangle$, where positive contribution forms on the leeward side and slight negative contribution on the windward side.

### Proper orthogonal decomposition analysis

To elucidate the type of turbulence events that result in the turbulence stresses shown in figure 6, we perform proper orthogonal decomposition (POD) of the flow fields around dominant surface waves identified previously. Here we employ 'snapshot POD' as per Sirovich [11], and its direct implementation to the velocity fields is explained below following Meyer *et. al.* [12]. Essentially, each fluctuation field can be reconstructed from the summation of the entire POD modes, $\psi = [\phi^1 \phi^2 \ldots \phi^N]$, multiplied by a series of unique coefficients (for each instance) $\mathbf{a}^n$,

$$\mathbf{u}^n = \sum_{i=1}^{N} a_i^n \, \phi^i = \psi \, \mathbf{a}^n, \tag{1}$$

To obtain the POD modes $\phi^i$, we first arrange the fluctuation $u'$ and $w'$ from a total of $N$ snapshots (here, 100 dominant waves)

$$\mathbf{U} = [\mathbf{u}^1 \mathbf{u}^2 \ldots \mathbf{u}^N] = \begin{bmatrix} u_1'^1 & u_1'^2 & \ldots & u_1'^N \\ u_2'^1 & u_2'^2 & \ldots & u_2'^N \\ \vdots & \vdots & \vdots & \vdots \\ w_1'^1 & w_1'^2 & \ldots & w_1'^N \\ w_2'^1 & w_2'^2 & \ldots & w_2'^N \\ \vdots & \vdots & \vdots & \vdots \end{bmatrix}, \tag{2}$$

and its autocovariance matrix $\widetilde{\mathbf{C}} = \mathbf{U}^T \mathbf{U}$ is used as input for an eigenvalue problem,

$$\widetilde{\mathbf{C}} \mathbf{A}^i = \lambda^i \mathbf{A}^i, \tag{3}$$

The solutions (both eigenvalues and eigenvectors) are ordered according to the size of the eigenvalues $\lambda_1 > \lambda_2 > \ldots > \lambda_N = 0$. The eigenvectors $\mathbf{A}^i$ become the basis for the POD modes $\phi^i$

$$\phi^i = \frac{\sum_{n=1}^{N} \mathbf{A}_n^i \, \mathbf{u}^n}{\| \sum_{n=1}^{N} \mathbf{A}_n^i \, \mathbf{u}^n \|}, \quad i = 1, 2, \ldots, N, \tag{4}$$

where the number of modes corresponds to the number of included snapshots. The POD coefficients can then be deter-

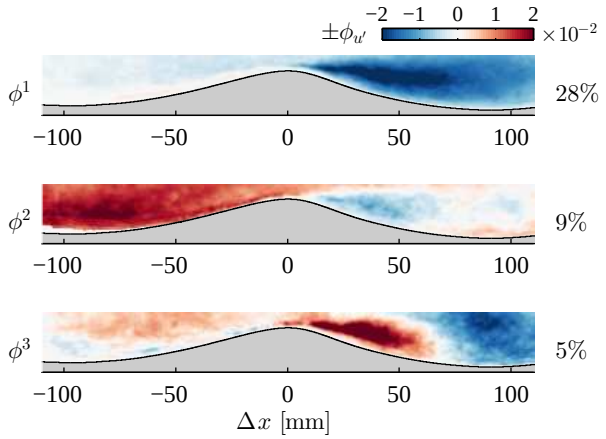


Figure 7: The first three (normalised) POD modes of the streamwise velocity fluctuation $u' = u - \langle U \rangle$, where the percentages show its contribution to the total turbulent kinetic energy.

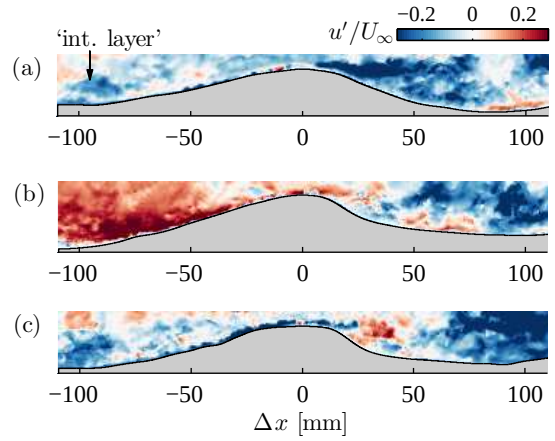


Figure 8: Examples of streamwise velocity fluctuation $u' = u - \langle U \rangle$, where POD mode 1, 2 and 3 are high.

mined from $\mathbf{a}^n = \psi^T \mathbf{u}^n$. In performing this analysis, we restrict our velocity snapshots to be within the roughness elements and slightly above the crest (see the domain of figure 7), otherwise the strongest mode will come from the very large scale turbulent motions in the outer part of the boundary layer.

Figure 7 shows the first three POD modes for streamwise velocity fluctuations, where the $+/-$ sign can be reversed by a negative coefficient. Since POD orders the eigenvalues and eigenvectors, the most energetic modes will be the few initial modes, which are typically associated with the larger-scale motions. Here we attempt to find the velocity instances where a particular mode is strong, which is marked by the high magnitude of the POD coefficient. Instances that nicely represent mode $\phi^{1-3}$ are shown in figure 8(a-c) respectively. It is clear that the difference between figure 8(a) and (b) is the existence of positive fluctuation on the windward side of the latter. Though not shown here, we can also plot the actual/total velocity $u = u' + \langle U \rangle$ and observe that new internal boundary layer (annotated in figure 8a), which also corresponds to lower velocity region, has been developed. On the other hand, POD mode $\phi^2$ represents the opposite. POD mode $\phi^3$ typically indicates small/broken separation events, which clearly shows the high-shear region downstream of the hill. These separation events dominate the flow over such hills or over wind-waves. Although higher order POD can be plotted, they correspond to smaller-scale motions, and the details of these smaller-scale flow features are beyond the scope of this paper.

## Conclusions

We conduct a large-view PIV measurement (covering over $2\lambda_0$) to characterise the turbulent boundary layer above young wind-generated waves. Our instantaneous velocity observations show that the entire boundary layer is affected by the surface waves, and strong flow separations occur downstream of most dominant waves. Within the separating flow, the wall-normal velocity fluctuations are dominated by smaller-scale coherence. The spatially-averaged velocity profile indicates a large velocity gradient below the wave crest, which occupies a significant proportion of the boundary layer. The conditionally-averaged flow field around the dominant waves show that turbulence stresses are indeed high downwind the wave crest. This occurrence indicates the highly varying form of the separation events, as suggested by the first few stronger POD modes. Mode 1 and 2 are differentiated by their uphill behaviour. POD mode 3 however, indicates small/broken separation events, combined with high-shear events downstream of the wave crest.

## Acknowledgements

The authors gratefully acknowledge the financial support from the Australian Research Council.

## References

[1] Donelan, M. A., Haus, B. K., Reul, N., Plant, W. J., Stiassnie, M., Graber, H. C., Brown, O. B. and Saltzman, E. S. On the limiting aerodynamic roughness of the ocean in very strong winds, *Geo. Res. Lett.*, **31**, 2004, L18306.

[2] Banner, M. L., Melville, W. K. On the separation of air flow over water waves, *J. Fluid Mech.*, **77**, 1976, 825–842.

[3] Kawai, S. Visualisation of airflow separation over wind-wave crests under moderate wind, *Boundary-Layer Meteorol.*, **21**, 1981, 93-104.

[4] Donelan, M. A., Hamilton, J. and Hui, W. -H. Directional spectra of wind-generated ocean waves, *Phil. Trans. R. Soc. Lond. A*, **315**, 1985, 509–562.

[5] Reul, N., Branger, H. and Giovanangeli, J. -P. Air flow structure over short-gravity breaking water waves, *Boundary-Layer Meteorol.*, **126**, 2008, 477–505.

[6] Zavadsky, A., Shemer, L. Characterization of turbulent airflow over evolving water-waves in a wind-wave tank, *J. Geo. Res.*, **117**, 2007, C00J19.

[7] Belcher, S. E., Hunt, J. C. R. Turbulent flow over hills and waves, *Annu. Rev. Fluid Mech.*, **30**, 1998, 507-538.

[8] Banner, M. L., Peregrine, D. H. Wave breaking in deep water, *Annu. Rev. Fluid Mech.*, **25**, 1993, 373–97.

[9] Chan, L., MacDonald, M., Chung, D., Hutchins, N., Ooi, A. A systematic investigation of roughness height and wavelength in turbulent pipe flow in the transitionally rough regime, *J. Fluid Mech.*, **771**, 2015, 743–777.

[10] Buckley, M. P., Veron, F. Structure of the airflow above surface waves, *J. Phys. Ocean.*, **46**, 2016, 1377-1397.

[11] Sirovich, L. Turbulence and the dynamics of coherent structures. Part I: Coherent structures, *Q. Appl. Maths.*, **45**, 1987, 561–571.

[12] Meyer, K.E., Pedersen, J. M. and Özcan, O. A turbulent jet in crossflow analysed with proper orthogonal decomposition, *J. Fluid Mech.*, **585**, 2007, 199–227.